

Water Resources Research

RESEARCH ARTICLE

10.1029/2019WR024935

Special Section:

Advances in remote sensing, measurement, and simulation of seasonal snow

Key Points:

- Snow line altitude (SLA) is automatically measured from Landsat TM/ETM+ scenes for a Himalayan catchment
- NDSI-based SLAs are validated against fSCA results and manual delineation from ALOS and Cartosat scenes
- Spatial and seasonal trade-offs in precipitation, temperature, and radiation are primary SLA controls

Supporting Information:

- Supporting Information S1

Correspondence to:

M. Girona-Mata,
mgirona29@gmail.com

Citation:

Girona-Mata, M., Miles, E. S., Ragettli, S., & Pellicciotti, F. (2019). High-resolution snowline delineation from Landsat imagery to infer snow cover controls in a Himalayan catchment. *Water Resources Research*, 55, 6754–6772. <https://doi.org/10.1029/2019WR024935>

Received 5 FEB 2019

Accepted 7 JUL 2019

Accepted article online 16 JUL 2019

Published online 14 AUG 2019

High-Resolution Snowline Delineation From Landsat Imagery to Infer Snow Cover Controls in a Himalayan Catchment

Marc Girona-Mata¹, Evan S. Miles², Silvan Ragettli³, and Francesca Pellicciotti^{2,4}

¹Institute of Environmental Engineering, ETH Zurich, Zurich, Switzerland, ²Swiss Federal Research Institute WSL, Birmensdorf, Switzerland, ³Hydrosolutions Ltd., Zurich, Switzerland, ⁴Department of Geography, Northumbria University, Newcastle upon Tyne, UK

Abstract The snow cover dynamics of High Mountain Asia are usually assessed at spatial resolutions of 250 m or greater, but this scale is too coarse to clearly represent the rugged topography common to the region. Higher-resolution measurement of snow-covered area often results in biased sampling due to cloud cover and deep shadows. We therefore develop a Normalized Difference Snow Index-based workflow to delineate snow lines from Landsat Thematic Mapper/Enhanced Thematic Mapper+ imagery and apply it to the upper Langtang Valley in Nepal, processing 194 scenes spanning 1999 to 2013. For each scene, we determine the spatial distribution of snow line altitudes (SLAs) with respect to aspect and across six subcatchments. Our results show that the mean SLA exhibits distinct seasonal behavior based on aspect and subcatchment position. We find that SLA dynamics respond to spatial and seasonal trade-offs in precipitation, temperature, and solar radiation, which act as primary controls. We identify two SLA spatial gradients, which we attribute to the effect of spatially variable precipitation. Our results also reveal that aspect-related SLA differences vary seasonally and are influenced by solar radiation. In terms of seasonal dominant controls, we demonstrate that the snow line is controlled by snow precipitation in winter, melt in premonsoon, a combination of both in postmonsoon, and temperature in monsoon, explaining to a large extent the spatial and seasonal variability of the SLA in the upper Langtang Valley. We conclude that while SLA and snow-covered area are complementary metrics, the SLA has a strong potential for understanding local-scale snow cover dynamics and their controlling mechanisms.

1. Introduction

The Himalayan mountains are the source of many major rivers in Southern Asia, supporting the water supplies of almost 800 million people (Bolch et al., 2012). Meltwater from snow and glaciers represents an important freshwater resource for drinking water, hydropower generation, and agricultural supply. Snow quantities, variability, and processes have often been disregarded in the region, with cryospheric studies generally focusing on the spectacular changes of the region's glaciers. However, studies have increasingly suggested that snow melt is of comparable importance to glacier melt for total runoff in the water balance of Himalayan high elevation catchments (e.g., Immerzeel et al., 2013; Lutz et al., 2014; Ragettli et al., 2015). Snow controls the seasonality of runoff by acting as a reservoir and reduces ice melt when the snow line is below the ablation area of glaciers. To understand the interactions between snow cover and local water resources, it is imperative to understand snow spatial distributions and the topographic and climatic controls of snow cover in mountain regions.

Snow cover controlling mechanisms vary at the local scale, and snow cover spatial variability increases with increasing resolution (Melvold & Skaugen, 2013). The strong variability of snow cover in high elevation catchments is related to the extreme topography, which affects both snow cover distribution and duration (Dedieu et al., 2014), and the complex gradients of precipitation (Collier & Immerzeel, 2015; Immerzeel et al., 2014), as well as melt patterns that might cause snow differential disappearance (Immerzeel et al., 2012). In addition, high interannual climate variability further increases spatial snow cover variations (Dedieu et al., 2014). In the Himalaya, the absolute magnitude and spatial variability of precipitation is mostly unknown at the catchment scale, due to coarse monitoring networks and the inability of regional or global atmospheric models to resolve local-scale processes including orographic shading

(Immerzeel et al., 2013). To some degree, these dynamics can be resolved with increasingly refined dynamic downscaling (Bonekamp et al., 2018; Collier & Immerzeel, 2015), but the lack of validation data makes it difficult to interpret results. At the catchment scale, observations of snow cover variability may allow more detailed investigations of local topographic controls and their relationship with climate. In this regard, remotely sensed snow cover data represent an alternative to meteorological station data, which are sparse in Himalayan high elevation catchments, and enable assessment of key processes affecting the temporal and spatial distribution of snow and thus hydrological storage.

Measuring the spatial extent and properties of snow has been a research priority for several decades. Multi-spectral satellite observations have been used since the first Landsat sensors were in operation (e.g., Rango & Lten, 1976). Numerous methods have been developed to exploit the spectral signature of snow (Dietz et al., 2012), usually exploiting the reflectance differences between the visible and near- or shortwave-infrared bands, first by spectral band ratios then through determination of the Normalized Difference Snow Index (NDSI) (Dozier, 1989). Spectral mixing methods were subsequently applied to utilize all spectral bands and determine subpixel snow coverage (e.g., Rosenthal & Dozier, 1996). This method has been advanced to consider the spectra of snow with different characteristics and extended operationally to global daily mapping of snow extent using the Moderate Resolution Imaging Spectroradiometer (MODIS; e.g., Painter et al., 2009). Parallel efforts have used passive or active microwave sensors to identify snow-covered areas (e.g., Burke et al., 1984; Shi & Dozier, 1993).

Previous studies have documented the influence of regional climate (e.g., Kapnick & Hall, 2011), topography (e.g., Deems, 2006), aspect (e.g., Jain et al., 2008), and vegetation (e.g., Pomeroy et al., 2009) on snow cover. However, the processes linking physiography, climate, and snow cover are nonlinear and difficult to characterize empirically. The variability in precipitation, temperature, and surface-atmosphere energy exchange complicates these relationships (Molotch & Meromy, 2014). Therefore, a key condition for identifying the complex controls on snow cover is a large sample size of observations (Molotch & Meromy, 2014). With the availability of multiyear satellite observations, statistical approaches have become less constrained by the sample size.

Spatial and temporal patterns in snow cover across Himalayan watersheds have been identified in previous studies (e.g., Dahe et al., 2006; Maskey et al., 2011; Mishra et al., 2013; Tahir et al., 2011; Wang et al., 2015). These studies have mostly focused on snow cover trends in response to climate change at the basin scale ($>5,000 \text{ km}^2$) with a relatively coarse spatial resolution ($\geq 250 \text{ m}$), which has difficulty representing snow cover dynamics at the catchment scale (Dietz et al., 2012). High-resolution (e.g., Landsat or Sentinel-2) satellite data offer the possibility to study local (catchment scale) variations of snow cover and statistically relate it to topographic metrics. A second problem is that commonly used snow cover metrics such as the snow cover area (SCA; e.g., Molotch & Bales, 2006; Molotch & Meromy, 2014) are spatial aggregations of the snow observations, limiting the spatial or temporal resolution of the analysis. These analyses therefore reduce information about fine-scale processes to bulk observations of change. Furthermore, SCA depends on the ability to map snow everywhere; thus, it is sensitive to clouds/shadows/vegetation and methodological biases in those areas.

The snow line altitude (SLA) is a valuable metric that integrates the competing effects of snow accumulation and melt; thus, it provides a holistic indicator for meteorological variations (Fausto & the PROMICE team, 2017). Due to the great impact topography has on weather and climate in the Himalaya, with elevation and aspect playing a major role on snow distribution and melt processes (Jain et al., 2008; Shea et al., 2015), SLA dynamics can show significant spatial and intraannual variability at the catchment scale, and this is attributable to both meteorological variability and direct topographic effects (Gurung et al., 2017).

Further knowledge on the SLA controlling mechanisms at the catchment scale, and their spatial and seasonal variability, is also key to assess the potential use of the SLA not only for glacier mass balance (e.g., Huss et al., 2013; Pelto, 2011; Shea et al., 2013) but also for hydrological modeling, allowing better characterization of snow cover and snow melt dynamics at the basin scale (Sorman et al., 2019).

Various approaches have been proposed to derive glacier SLAs from remotely sensed products (e.g., Klein & Isacks, 1999; McFadden et al., 2011; Prantl et al., 2017; Seidel et al., 1997), often as a proxy for the glacier equilibrium line altitude, by either taking advantage of the fact that the snow line often appears as a sharp discontinuity in spectral albedo that separates the accumulation from the ablation zone (Klein & Isacks, 1999),

exploring the snow line as a statistical concept (i.e., 50% of SCA) (Seidel et al., 1997), using supervised classification to delineate the snow ice boundary (McFadden et al., 2011), or using other, often high-resolution, methods (e.g., camera, radar, and Terrestrial Laser Scanner) to observe snow line variations for small areas (e.g., Prantl et al., 2017). However, none of these have attempted to delineate snow lines or analyze their variability at the catchment scale.

To observe local changes in snow cover and thus infer the topographic and climatic controls of snow processes, we determine the SLA as derived from historic Landsat Thematic Mapper (TM) and Enhanced Thematic Mapper+ (ETM+) observations. We take advantage of 15 years of frequent observations to measure temporal and spatial patterns. We develop an automated algorithm that delineates the transient snow line at a 30-m resolution from atmospherically-corrected Landsat scenes in the upper Langtang Valley (350 km²), in Nepal. This algorithm uses the NDSI to map snow-covered area, and it takes into account confounding factors in the scene, such as cloud, shadow, high-altitude ranges, and rock outcrops, to provide a measurement of the altitudinal extent of consistent snow cover. We validate the NDSI-derived snow-covered areas for three scenes against subpixel snow cover fraction data derived from spectral unmixing and independent high-resolution data sets. In combination with topographic variables calculated from a 30-m digital elevation model (DEM) and modeled radiation receipts, we obtain a data set of descriptive attributes for every observed snow line point (SLP; including position, altitude, slope, aspect, or clear-sky incoming shortwave radiation) that we use to characterize possible causes of the observed variability.

To our knowledge, this is the first study that attempts to describe the mechanisms governing snow cover dynamics at a 30-m spatial resolution for a Himalayan catchment.

Applying the SLA algorithm, our research aims to:

1. determine historical snow lines from Landsat data;
2. characterize the seasonal pattern of snow cover and SLA in the valley;
3. determine local SLA differences based on aspect and their consistency between seasons;
4. measure the differences in SLA between the subcatchments of the valley; and
5. identify processes controlling the seasonal and spatial variability of SLA for Himalayan catchments.

2. Study Site

The Langtang River catchment is located in the monsoon dominated central Nepalese Himalayas. It lies 50 km north of Kathmandu, abutting the Tibetan Autonomous Republic of China. This study focuses on the upper reaches of the Langtang River catchment, with outlet near Kyanjing village (Figure 1). This portion of the catchment measures 350 km² and is 31% glacierized, with 24% of the glacier area mantled by rocky debris (Pellicciotti et al., 2015). The catchment contains several debris-covered glaciers as well as the debris-free benchmark Yala Glacier.

2.1. Climate

The climate in this region of the Himalaya is dominated by monsoon circulation with easterly winds in summer and westerly winds from October to May. In the Langtang Valley, based on mean values over the period from 1957 to 2002, 77% of annual precipitation occurs during the months of June to September (Uppala et al., 2005). However, recent studies instead suggest four distinct seasons (e.g., Immerzeel et al., 2014). The pre-monsoon season lasts from March to mid-June and is characterized by a gradual increase of air temperature with high diurnal temperature variations, with few and small precipitation events recorded. A progressive transition to the monsoon (mid-June to September) takes place during the second half of premonsoon (Heynen et al., 2016; Shea et al., 2015). During the monsoon, daily precipitation events occur. Air temperature is above freezing across most of the valley but has low diurnal variability, mainly due to thick and persistent cloud cover that attenuates fluctuations controlled by solar radiation. In the latter part of monsoon, the frequency of precipitation events considerably decreases (Shea et al., 2015). Weather patterns clear leading into the postmonsoon (October–November), which has almost no precipitation and a gradual decrease in air temperatures, while diurnal temperature fluctuations are comparable to the premonsoon. The winter season (December to February) has the lowest temperatures of the year, which lower the freezing level, and occasional but extreme precipitation events of a higher magnitude (Immerzeel et al., 2014; Heynen et al., 2016; Shea et al., 2015; Shiraiwa et al., 1992). Precipitation in winter is caused by westerly troughs but also associated with the existence of widespread snow cover (Seko, 1987), and it is characterized

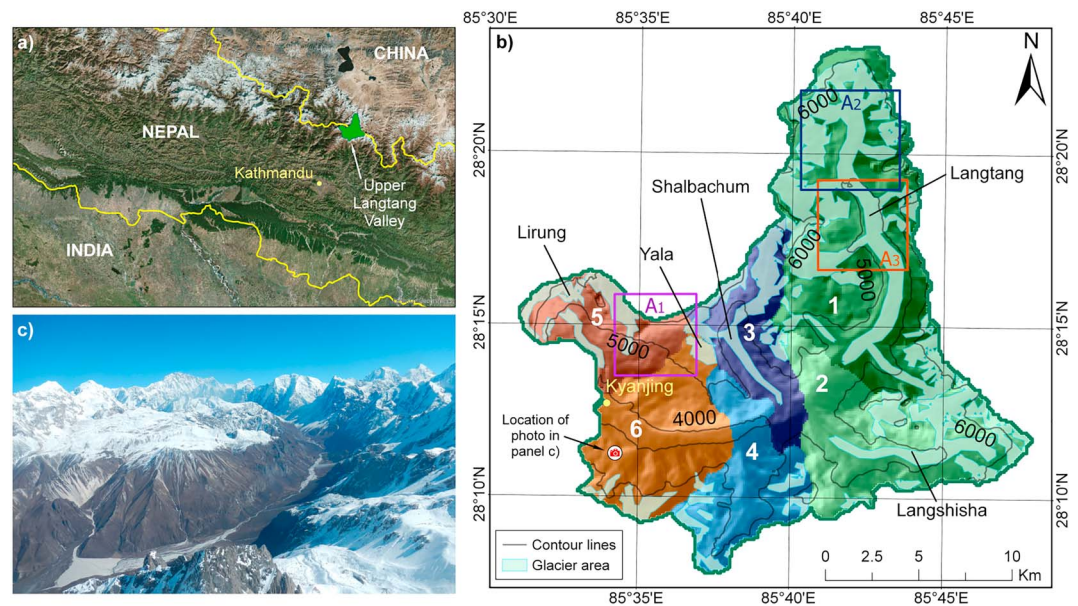


Figure 1. (a) Location of the upper Langtang Valley; centered on $85^{\circ}40'00''$ E, $28^{\circ}14'00''$ N. (b) Map of the derived study subcatchments in the upper Langtang Valley, with location of Kyanjing (28.208° N, 85.574° E) and main glaciers indicated. (c) Picture of the main valley (i.e., low portions of subcatchments 2, 3, and 4) of the upper Langtang Valley as seen from its southwestern corner (within subcatchment 6) at $\sim 4,500$ m. Fine aspect differences are apparent on the narrow ridges directly across the valley, while larger-scale differences between the right and left sides of the picture (north and south aspects) are especially pronounced due to solar exposure.

by very large interannual variability (Seko & Takahashi, 1991). Depending on the year, it may result in a heavy snowfall in the upper valley, lowering the snow line dramatically (Morinaga et al., 1987). The starting time of premonsoon temperature increase also exhibits high interannual fluctuations (Morinaga et al., 1987).

Due to the extreme topography, substantial spatial variation in the magnitude and frequency of the precipitation events is observed at both the macro and local scales (Shrestha & Aryal, 2010). The small distance between Kathmandu and the Langtang Valley results in very different seasonal distributions of precipitation: the nonmonsoon to monsoon precipitation ratio is 0.14 in Kathmandu but 0.66 in the Langtang Valley (Seko, 1987). Precipitation is also dependent on altitude (Immerzeel et al., 2014; Seko, 1987), but the relationship is complex (Collier & Immerzeel, 2015). The strong local wind circulations, induced by orographic changes at the large scale, explain this significant variation of the regional climatic conditions (Yasunari & Inoue, 1978). At the same time, both the altitudinal and horizontal precipitation gradients have a high degree of seasonal variability (Immerzeel et al., 2014). According to Seko (1987), precipitation in the Langtang Valley decreases with altitude from June to September, whereas this correlation is positive from December to March.

Lower precipitation and higher air temperatures are registered in the upper parts of the Langtang Valley during the monsoon, which suggests a negative precipitation gradient from the southwest toward the north-eastern part of the valley. This gradient is attributed to the extreme topography acting as a natural barrier (Shiraiwa et al., 1992). Consequently, glaciers at the highest elevations (northeast part of the catchment) receive less snow throughout the entire year, accentuating the equilibrium line altitude regional differences within the valley (Benxing et al., 1984; Shiraiwa et al., 1992). The upper Langtang Valley shows a heterogeneous spatial pattern of mass balance, supporting the idea that precipitation is also heterogeneous within a relatively small catchment (Pellicciotti et al., 2015).

3. Data

This study uses Level-1 top-of-atmosphere data from Landsat missions 5 TM and 7 ETM+ for the period 1999–2013. After filtering the archive to reduce problems with cloud cover, we analyzed 194 scenes for path

Table 1
Threshold Values Used in the Snow Line Delineation Algorithm

Threshold	Value
NDSI	0.45
High-altitude snow line points	5,700 m.a.s.l.
Closed small snow-free areas (i.e., outcrops)	0.15 km ²
Snow line points per subcatchment	500 points
Snow line points per subcatchment and aspect range	100 points

Note. NDSI = Normalized Difference Snow Index.

141, row 40. All scenes with >50% cloud cover over the Langtang Valley as well as additional scenes, where the clouds significantly obscured the valley's glaciers, were removed from the sample.

We used the CGIAR Consortium for Spatial Information (CGIAR-CSI) void-filled DEM (Jarvis et al., 2008) generated from NASA's Shuttle Radar Topography Mission at 90-m resolution to represent topography at the study site. The CGIAR-CSI void-filled DEM was resampled to 30-m resolution using spline interpolation (Her et al., 2015) and the exact footprint of the Landsat imagery.

Clear-sky global irradiance was simulated with a nonparametric model based on Iqbal (1983) accounting for the position of the Sun relative to every model grid cell at each time step, as in Ragetti et al. (2015). The vector algebra approach proposed by Corripio (2003) was used for the interaction between the solar beam and terrain morphology.

Observed daily precipitation data in Kyanjing (Figure 1) for the study period (1999–2013) were aggregated to obtain mean monthly records. We then used previously derived horizontal and vertical precipitation gradients for the upper Langtang Valley (Immerzeel et al., 2014) to extrapolate Kyanjing precipitation records across the valley and aggregated these values to produce a mean monthly value for each subcatchment.

Similarly, we used hourly records of air temperature, measured in Kyanjing from May 2012 to December 2014, along with seasonal temperature lapse rates measured in the valley (Heynen et al., 2016), to estimate monthly freezing line altitudes near Kyanjing and aggregate these to monthly values.

4. Methods

4.1. Snow Line Determination

The Landsat Level-1 top-of-atmosphere digital numbers were atmospherically corrected to surface reflectance values with the LandCor implementation (Zelazowski et al., 2011) of the 6S radiative transfer model (Kotchenova & Vermote, 2007). The exact implementation is described in Miles et al. (2017), and it allows a pixel-by-pixel radiometric adjustment of the entire Landsat scene based on spatial representations of ozone, water vapor, and aerosol optical depth based on satellite global observations. Numerous methods have been developed to map snow from multispectral satellite data (Dietz et al., 2012). We selected the established and computationally efficient NDSI (for Landsat 5/7,
$$\text{NDSI} = \frac{\text{Band2}(0.52-0.60\mu\text{m}) - \text{Band5}(1.55-1.75\mu\text{m})}{\text{Band2}(0.52-0.60\mu\text{m}) + \text{Band5}(1.55-1.75\mu\text{m})}$$
) method to map snow. Relative to more advanced methods such as spectral mixing, the NDSI method is prone to erroneous classification in areas of deep shadow and vegetation (Rittger et al., 2013). However, our study area has limited vegetative cover and tests have indicated that deep shadows in the Himalayan region are problematic for even spectral mixing approaches (Rittger et al., 2013).

Determination of the appropriate NDSI threshold value poses a key challenge for this method. Although the NDSI snow threshold is temporally and spatially variable at the local (scene) scale (Burns & Nolin, 2014), particularly when applied to higher-resolution products (e.g., Landsat; Härer et al., 2018), many studies have nonetheless assumed snow to be present if the NDSI exceeds a uniform value, for example, $\text{NDSI} \geq 0.4$ (Hall et al., 1995). NDSI has been most commonly applied using thresholds ranging 0.35–0.55 (Burns & Nolin, 2014). Prior research has suggested that, in the Himalayas, NDSI values for water may be above 0.4 but not higher than 0.45 (Kulkarni et al., 2006). Based on this and the close interscene agreement of the LandCor/6S-corrected at-sensor reflectance values, we applied a uniform NDSI threshold of 0.45 (Table 1) to determine the snow-covered area. This is within the range of typical values and avoids misclassification of water as snow. In addition, our processing also determined coverages of clouds and deep shadows for each scene.

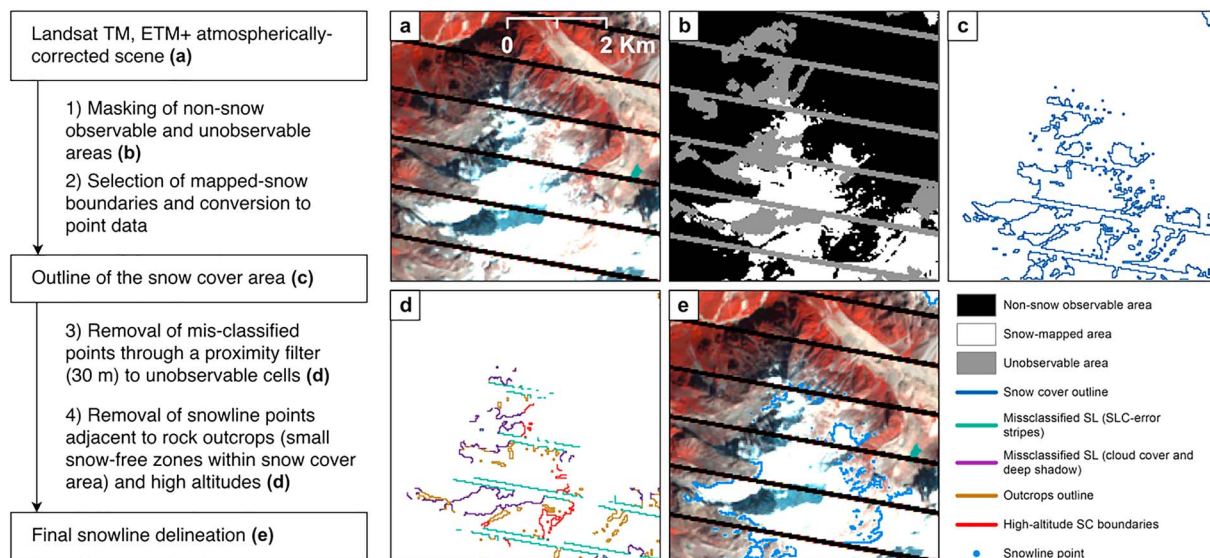


Figure 2. Snow line delineation process, including pictures of (a) subset of a Landsat atmospherically-corrected scene (6 October 2012 Landsat ETM+ scene; false-color composite with bands 4, 3, 2), (b) masking of nonsnow and unobservable areas, (c) outline of the snow-covered area, (d) misclassified snow line points to be removed, and (e) final snow line delineation. TM = Thematic Mapper; ETM+ = Enhanced Thematic Mapper; SL = snow line; SLC = scan line corrector.

Based on the classified images, we calculated the observable SCA, at the catchment and subcatchment scales, as the ratio of the SCA to the observable area, the area of analysis after removal of known errors. Specifically, the confounding effects of cloud cover, deep shadows, steep cliffs, high-altitude areas, and ETM+ scan line corrector (SLC) error stripes may obscure parts of the snow-covered area and create incorrect snow outlines. Our automated workflow eliminated these errors and delineated the snow line across the study area (Figure 2).

First, the boundaries of the Landsat-mapped snow cover were determined and converted from raster to point data. The snow line is theoretically equivalent to this outline, but the snow-covered area may not be fully visible or may include internal snow-free areas, so the observed snow margin bordering obscured areas (clouds, shadows, SLC-error stripes, etc.) may be misidentified as the snow cover outline. Thus, in the second step, we removed these locations through a proximity filter, removing SLPs within 30 m (one cell width) of these data types. In the third step, we removed snow boundaries due to rock outcrops, which also do not represent meteorological patterns. To do so, closed small snow-free zones ($<0.15 \text{ km}^2$ —threshold determined upon visual observation of the scenes) within the snow-covered area and all SLPs at very high altitude ranges ($>5,700 \text{ m.a.s.l.}$) were removed (Table 1). The high-altitude threshold (above which SLPs were not considered to be part of the snow line) was chosen based upon the highest altitudes where transient snow lines are observed throughout the year. In the Langtang Valley, the highest transient snow lines sit above the equilibrium line altitude of glaciers, which lies approximately at $5,400 \text{ m.a.s.l.}$ (Ragettli et al., 2015).

As an output from this workflow, we obtained a point data set for each scene corresponding to the snow boundary pixel locations, which described the observable portion of the snow line. To interpret the spatial patterns of SLA, we then calculated a range of attributes for each point of the derived snow line. These included spatial coordinates (UTM Easting and Northing); altitude, slope, and aspect derived from the DEM; and modeled clear-sky shortwave daily radiation receipts.

Subsequently, the upper Langtang Valley was divided into six subcatchments to examine broad spatial patterns (Figure 1b). These catchments were delineated from the DEM using drainage modeling (Arc Hydro Tools), and their terrain characteristics are described in Table 2. The catchments are roughly aligned in a 3×2 pattern, enabling determination of differences in the north-south and east-west directions (Figure 1b). Finally, the SLPs were further aggregated for each subcatchment into four groups based on general aspect: east ($45\text{--}135^\circ$), south ($135\text{--}225^\circ$), west ($225\text{--}315^\circ$), and north ($315\text{--}45^\circ$). These groupings of the SLA data allowed us to consider the roles of potential controls of the snow line and how they vary spatially within the study basin. In order to ensure comparability and consistency of the results, we used the number of derived

Table 2
Terrain Characteristics at Each Subcatchment

Parameter	Units	Subcatchment					
		1 - NE	2 - SE	3 - NC	4 - SC	5 - NW	6 - SW
Area	km ²	121.2	66.85	35.06	38.83	31.83	52.12
	%	35.05	19.33	10.14	11.23	9.21	15.04
Glacierized area	km ²	55.79	20.96	12.93	5.86	9.65	5.02
	%	46.03	31.35	36.88	15.09	30.32	9.64
Mean slope	%	26.87	29.83	30.22	25.90	31.60	24.44
Mean elevation	m.a.s.l.	5437.99	5300.56	5146.19	4983.46	5187.60	4576.56
Elevation range	m.a.s.l.	4401–7120	4120–6898	3977–6694	3934–6352	3885–7178	3754–5848
East aspect (45–135°)	%	26.62	15.31	27.52	26.37	27.03	16.00
South aspect (135–225°)	%	28.55	27.21	34.03	24.39	50.60	26.43
West aspect (225–315°)	%	28.27	29.02	28.35	25.57	19.14	16.61
North aspect (315–45°)	%	16.56	28.45	10.10	23.67	3.24	40.96

Note. Subcatchments are identified as in Figure 1b, along with their relative location within the catchment.

SLPs as a data quality metric to assess the extent of the snow line sample extracted from each aggregation (i.e., scene, subcatchment, and aspect).

Lastly, while vegetation has been recognized to play a role on snow cover occurrence and persistence (e.g., Pomeroy et al., 2009), we did not include vegetation in our analysis since it occurs at lower elevations than those where the snow line is generally observed in the upper Langtang Valley.

4.2. Limitations

The overall method approach used in this study to derive SLAs is subject to some limitations, which are either inherent to the data (Landsat TM, ETM+ products) or the snow cover mapping method (NDSI), such as the omission of shadowed areas, use of a binary classification technique, or the saturation of the Landsat-sensor visible bands.

While shadowed areas account for a minor fraction of most of the Landsat scenes used in this study, their omission may have introduced a bias in our results especially for north-aspect slopes. This also applies to areas persistently affected by cloud cover and SLP-error bands, and it can lead to consistent under or overestimations. These biases can normally be, at least partially, mitigated by using spectral unmixing techniques, which are able to map snow cover within shadowed areas. However, deep and prevalent shadows in the Himalaya tend to present a problem to any classification technique, including spectral unmixing (e.g., Klein & Isacks, 1999; Rittger et al., 2013).

The ability of spectral unmixing methods to retrieve the snow cover at the subpixel scale (fSCA) is very advantageous for the purpose of mapping and quantifying the extent of snow cover. However, to delineate snow lines as we propose, a binary (snow/nonsnow) pixel classification is eventually inevitable, that is, to determine the snow cover outline. In this regard, for vegetation-free areas, NDSI, and spectral unmixing (using 50% fSCA threshold for snow/nonsnow pixel classification) yield similar results (Rittger et al., 2013).

Sensor saturation of the visible bands is an intrinsic limitation of Landsat TM, ETM+ products for their use in snow cover mapping. As such, this may have introduced some bias in our results. However, channel saturation does also, to some extent, limit the effectiveness of spectral unmixing techniques (Painter et al., 2009).

Therefore, while spectral unmixing techniques are generally capable of, at least partially, overcoming these limitations, the characteristics of Himalayan watersheds significantly hinder the ability of spectral unmixing techniques to overperform NDSI binary classification.

4.3. Validation

Motivated by the discussed method limitations and concerns, we assessed the performance of both the snow cover mapping and the snow line delineation methods used in this study.

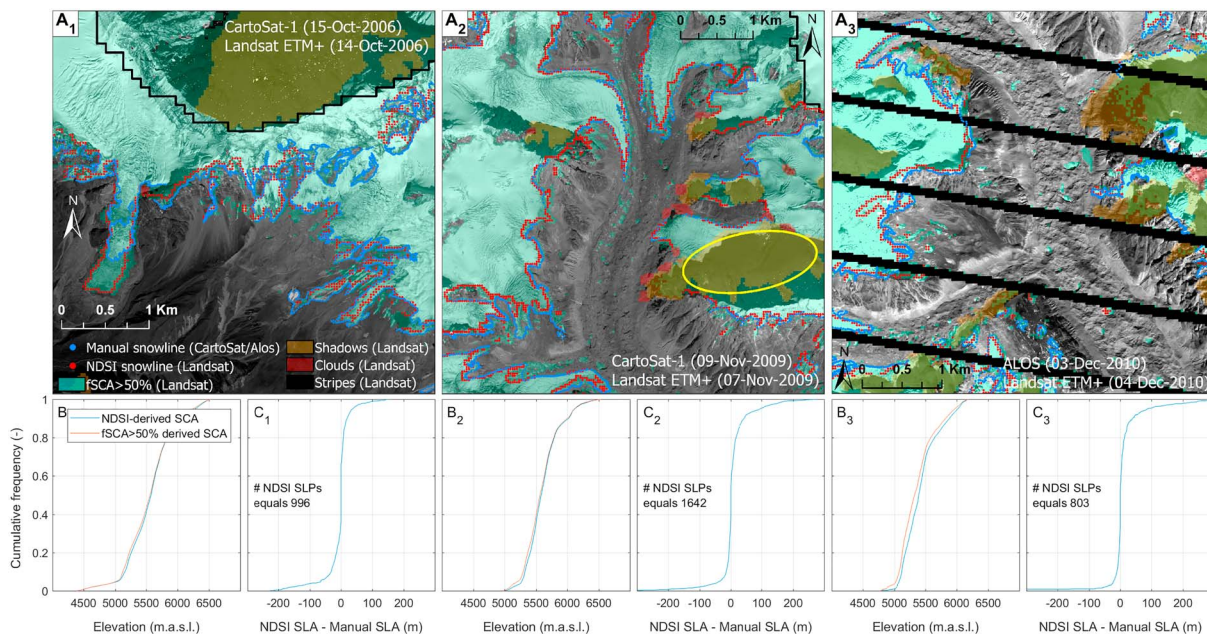


Figure 3. ($a_{1,2,3}$) Validation of NDSI automatically derived snow lines from three Landsat scene subsets (see label in each panel) with manually-derived snow lines from high-resolution satellite products (shown as background images) corresponding to similar dates. Shadow (e.g., see yellow oval in panel a_2), cloud, and error striping areas are masked and excluded from validation. Binary SCA derived using spectral unmixing and the threshold $fSCA \geq 0.5$ are also shown for comparison. ($b_{1,2,3}$) Cumulative distribution functions (CDF) of SCA with elevation; comparison between SCAs derived using the NDSI method and spectral unmixing with the threshold $fSCA \geq 0.5$ for the scene subsets shown in panels $a_{1,2,3}$ respectively. ($c_{1,2,3}$) CDFs of the difference between NDSI-derived SLA values and their closest manually-derived SLA value, corresponding to the scene subsets shown in panel ($a_{1,2,3}$) respectively. ETM+ = Enhanced Thematic Mapper; NDSI = Normalized Difference Snow Index; SCA = snow cover area; SLA = snow line altitude; SLP = snow line point.

First, we compared binary SCAs derived using the fixed-threshold NDSI and fractional SCAs (fSCA) determined using spectral unmixing techniques (e.g., Dietz et al., 2012; Painter et al., 2009; Rittger et al., 2013; Rosenthal & Dozier, 1996). For this approach, we used four spectral end-members from Klein and Isacks (1999) and Painter et al. (2009) to characterize the anticipated reflectance of homogeneous covers of snow (general), ice, rock, and vegetation. Following an iterative approach, weighted combinations of these spectra were optimized to find the subpixel combination of land covers best reproducing the 6S-corrected surface reflectance values at each pixel. We then calculated the basin-wide fSCA by summing the subpixel fractional snow cover for the region of interest. We also determined a binary snow cover product from the unmixing results based on pixels with at least 50% subpixel snow cover, representing the ideal output from the NDSI calculation. This approach was applied to three ETM+ scenes collected on 14 October 2006, 7 November 2009, and 4 December 2010 and compared to the NDSI results in terms of SCA and snow line accuracy, to evaluate the NDSI-based snow line delineation.

Second, in order to validate the snow line mapping methodology, snow lines were manually delineated from independent high-resolution orthoimages in close temporal correspondence to the three dates listed above and compared to the SLPs automatically delineated from Landsat imagery. Specifically, we manually derive snow lines from two CartoSat-1 orthoimages (2.5-m resolution) dated 15 October 2006 and 9 November 2009, as well as an Advanced Land Observation Satellite (ALOS) Panchromatic Remote-sensing Instrument for Stereo-Mapping (PRISM) orthoimage (2.5-m resolution) dated 3 December 2010. Details of the stereo image analysis and orthoimage generation can be found in Ragetti, Bolch and Pellicciotti (2016). We used different subsets of the upper Langtang Valley (Figure 1) to undertake the validation with each of the high-resolution orthoimages (Figure 3 $a_{1,2,3}$). Shadow, cloud, and SLC-error striping areas were masked and excluded from the validation data set in both method validations.

4.4. Analysis

Derived snow lines were analyzed for seasonal and spatial patterns in terms of mean altitude and seasonal ranges. Seasonal snow cover frequency was analyzed with respect to elevation to assess SLA stability.

First, we processed the raw snow cover data to assess the proportion of observations indicating snow cover at different altitudes. Taking into account the entire Landsat record for the study period (1999–2013), for each

Table 3

Comparison Between NDSI and Spectral Unmixing (Benchmark) Derived SCA for Three Landsat Scenes, Using Error and Information Retrieval Metrics (i.e., Precision, Recall, Accuracy, F Score, and Commission and Omission Errors as Defined in, e.g., Rittger et al., 2013)

Date	Metric	Subcatchment					
		1 - NE	2 - SE	3 - NC	4 - SC	5 - NW	6 - SW
14 Oct 2006	Deep shadows (%)	7.2	10.6	7.5	8.1	0.7	7.4
	Precision	0.99	0.99	0.99	0.99	0.99	0.99
	Recall	0.79	0.76	0.83	0.76	0.87	0.79
	Accuracy	0.86	0.84	0.92	0.86	0.92	0.94
	F score	0.88	0.86	0.91	0.86	0.92	0.88
	Recall (excl. shadows)	0.86	0.88	0.88	0.86	0.87	0.89
	Accuracy (excl. shadows)	0.91	0.92	0.94	0.92	0.92	0.97
	F score (excl. shadows)	0.92	0.93	0.93	0.92	0.93	0.94
	Commission error	0.09	0.08	0.12	0.09	0.17	0.07
	Omission error	0.32	0.34	0.19	0.26	0.19	0.12
	Omission error (excl. shadows)	0.25	0.22	0.16	0.27	0.18	0.08
07 Nov 2009	Deep shadows (%)	13.5	22.7	12.6	20.1	3.3	19.5
	Precision	0.99	0.99	0.99	0.98	0.99	0.99
	Recall	0.70	0.58	0.77	0.56	0.84	0.57
	Accuracy	0.82	0.75	0.89	0.79	0.92	0.89
	F score	0.82	0.73	0.87	0.71	0.91	0.73
	Recall (excl. shadows)	0.86	0.85	0.88	0.80	0.86	0.89
	Accuracy (excl. shadows)	0.92	0.92	0.94	0.91	0.93	0.98
	F score (excl. shadows)	0.92	0.91	0.93	0.88	0.92	0.94
	Commission error	0.08	0.07	0.09	0.09	0.13	0.06
	Omission error	0.33	0.38	0.22	0.30	0.18	0.18
	Omission error (excl. shadows)	0.21	0.19	0.16	0.16	0.17	0.08
04 Dec 2010	Deep shadows (%)	18.7	31.7	16.5	29.4	4.8	27.9
	Precision	0.99	0.99	0.99	0.98	0.99	0.98
	Recall	0.65	0.48	0.70	0.42	0.83	0.40
	Accuracy	0.80	0.71	0.86	0.79	0.91	0.87
	F score	0.79	0.65	0.82	0.59	0.90	0.56
	Recall (excl. shadows)	0.85	0.82	0.83	0.81	0.85	0.85
	Accuracy (excl. shadows)	0.92	0.91	0.91	0.95	0.92	0.98
	F score (excl. shadows)	0.92	0.90	0.90	0.89	0.91	0.91
	Commission error	0.18	0.17	0.21	0.16	0.24	0.12
	Omission error	0.35	0.40	0.25	0.26	0.19	0.17
	Omission error (excl.shadows)	0.21	0.19	0.19	0.12	0.18	0.08

Note. NDSI = Normalized Difference Snow Index; SCA = snow cover area.

pixel we determined the seasonal snow cover frequency as the ratio between snow cover occurrences and observable occurrences. We then determined the mean and standard deviation of the seasonal snow cover frequency values for 100-m elevation bins spanning the range of elevations at the study site. This method highlights the transition from areas rarely covered by snow (low frequency) to zones regularly covered by snow (high frequency), with the width of that transition representing the range of altitudes of the transient snow line for that season, that is, the SLA stability.

Second, we calculated various SLA statistics (i.e., mean, median, and standard deviation) at the sub-catchment and whole catchment scales for each Landsat scene. To evaluate the SLA spatial and seasonal variability, SLA statistics encompassing the full study period (1999–2013) were also aggregated seasonally.

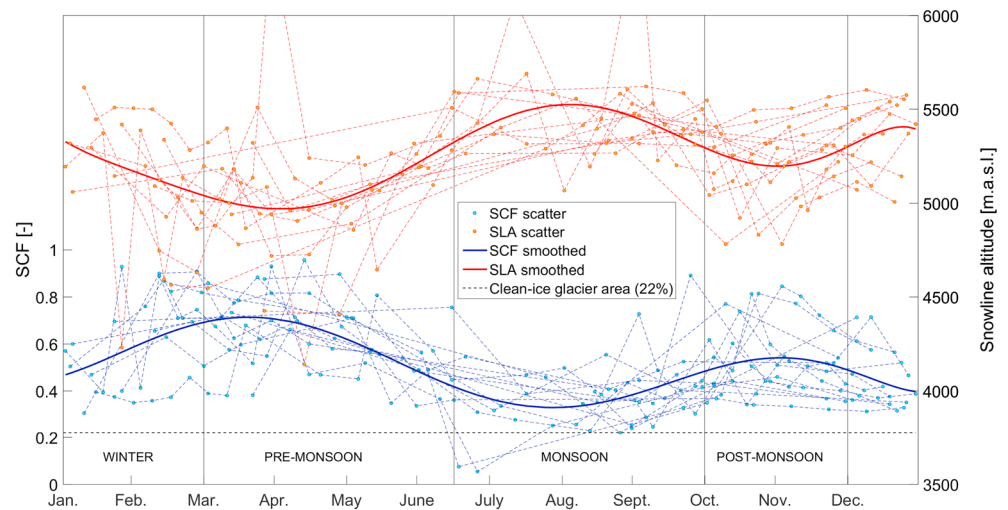


Figure 4. Annual series of mean SLA and SCA values derived from 194 Landsat scenes over the period 1999–2013. SLA = snow line altitude.

As different portions of each scene are affected by clouds, shadows, and SLC-error stripes, we conducted the analysis at the subcatchment scale by selecting only the scenes with a minimum number of derived SLPs in that subcatchment. We used a trial and error approach to determine this threshold, which was set to 500 SLPs at the subcatchment scale. Similarly, only the scenes with at least 100 SLPs per aspect range within each subcatchment were selected to study aspect-related differences. This results in a different number of scenes available for each subcatchment and aspect range but ensures that the SLA values included in the analysis are statistically and spatially representative.

We grouped the subcatchments in terms of latitudinal (north or south) and longitudinal (west, center, or east) positions to highlight broad spatial patterns between the subcatchments. To assess the fine spatial variability, we determined the mean-scene SLA difference between opposing aspect quadrants (north-south and east-west) for each subcatchment.

5. Results

5.1. Results From Validation

5.1.1. Comparison of NDSI and fSCA Results

The spectral unmixing and NDSI approaches yielded very comparable snow cover maps through most of the study site, with the exception of deep shadows and clean-ice ablation areas. Our NDSI analysis masked areas of deep shadow due to the very low at-sensor radiance values for these locations, which effectively reduced the strength of the spectral signal relative to noise. This problem is especially troublesome for the Himalaya (e.g., Klein & Isacks, 1999; Rittger et al., 2013) and for the 8-bit radiometric resolution of ETM+ data but may reduce for Landsat 8's OLI data (16 bit) or Sentinel-2's MSI (12 bit). Nonetheless, the spectral unmixing approach was able to identify snow in some zones of deep shadow (e.g., Figure 3a). Spectral unmixing was also more successful than NDSI in differentiating between snow and bare ice in glacier ablation areas, where NDSI values were often above 0.45. Other studies have successfully differentiated between snow and ice using NDSI, but this was difficult to achieve for the large population of study scenes.

These factors led to a substantial difference in total SCA (see commission error and omission error metrics in Table 3) for the study area as estimated by fSCA and NDSI approaches. However, eliminating masked shadow areas from the fSCA results, we find nearly identical snow-covered areas and high values for information retrieval metrics (see precision, recall, accuracy and F score in Table 3), suggesting that the NDSI approach is very accurate in the zones that we have evaluated it. Subsequent comparison with high-resolution optical imagery (section 5.1.2) suggests that the fSCA approach erroneously mapped some shadows as snow, supporting the removal of these areas from the study domain. Overall, the snow line errors induced by using a fixed NDSI value (rather than, e.g., a spectral unmixing approach) were very minor (Figure 3b_{1,2,3}).

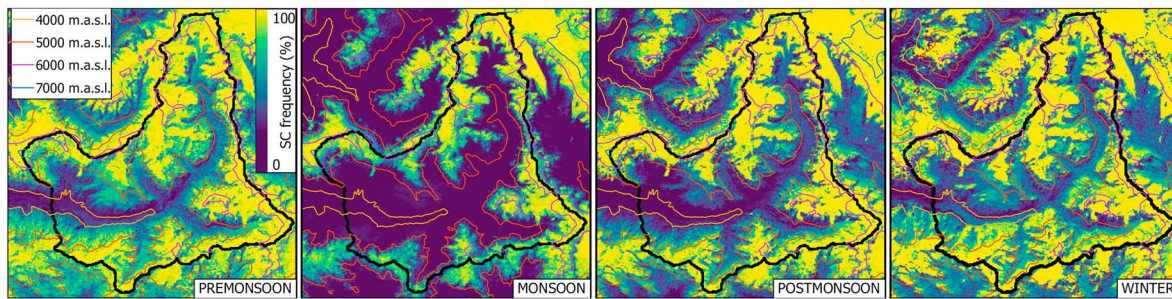


Figure 5. Seasonal snow distribution in the upper Langtang Valley, expressed as the frequency of snow cover for each pixel based on the full population of scenes for each season.

5.1.2. Comparison of Landsat and Higher-Resolution Orthoimage SLPs

Snow lines automatically derived from Landsat imagery using the NDSI analysis have very close correspondence to those manually delineated from higher-resolution orthoimages. Differences in altitude between NDSI-derived SLPs and manually-drawn SLPs are low and consistent across the study region. Negative and positive SLA differences are similar in frequency and magnitude, and more than 90% of NDSI SLPs are within 100 m in altitude of the closest manually-derived SLP (Figure 3b_{1,2,3}). By filtering out snow lines outlining rock outcrops, our NDSI automatic method has occasionally discarded SLPs surrounding small snow-free areas that are not outcrops but instead relate, at least partially, to climate factors (Figure 3a₁).

5.2. Snow Line Seasonal Patterns and Stability

Mean SLA and SCA values for all available scenes show a strong seasonal pattern in spite of high scattering (Figure 4). Lows in SLA are apparent in premonsoon and, to a lesser extent, in winter, while high SLA values occur in the monsoon and again in December. As expected, we observe that the SCA behavior is opposite to SLA variations over the entire year. The lowest SCA values, spread over the entire year, are rarely below 22%, which is approximately the clean-ice glacier area in the upper Langtang Valley (Ragettli et al., 2015).

The seasonal patterns are also evident in Figure 5, which shows the frequency of snow observation at each pixel location. Of the seasons, premonsoon has the highest frequency of snow cover for the valley bottoms. During the monsoon, snow cover is reduced essentially to the clean-ice areas of the basin's glaciers. The postmonsoon shows an intermediate valley-bottom snow cover frequency. In winter, snow is common even at the lowest elevations. Snow deposition on avalanche cones beneath steep rock faces is apparent in all seasons but most evident for the monsoon, when these locations are below the seasonal snow line. These results suggest that snow cover spatial variations within a season might be comparable to those between different seasons and that the magnitude of the spatial variability does also vary from one season to another.

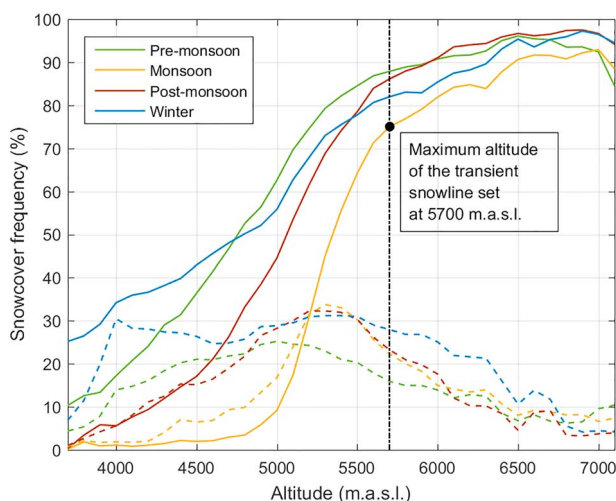


Figure 6. Seasonal snow cover frequency in the upper Langtang Valley. Dotted lines correspond to standard deviation values.

While snow cover frequency continuously rises with altitude for all seasons, there exist differences in the snow cover presence for low altitudes and the slope of the transition from low to high frequency (Figure 6). The frequency of snow cover gradually increases in winter, starting at 25% in the lowest elevation range (3,700 m) and reaching more than 90% of frequency at 5,700 m. In the monsoon a step change in snow cover frequency occurs at 5,000–5,600 m, suggesting that this is a common transition between snow-covered and snow-free terrain during this season. Finally, premonsoon and postmonsoon exhibit similar trends, with a slightly steeper snow cover frequency increase in postmonsoon and higher snow presence in low-altitude ranges for premonsoon. With respect to the SLA, monsoon is the most stable season, followed at a considerable distance by postmonsoon, premonsoon, and winter, respectively.

This seasonal variability in snow line stability is further highlighted by the mean seasonal SLA ranges (Figure 7). Overall, the premonsoon experiences both an initial increase and a rapid decline in snow cover and the snow line rapidly progresses from its annual minimum to monsoon values (Figure 4), resulting in a consistent snow line position

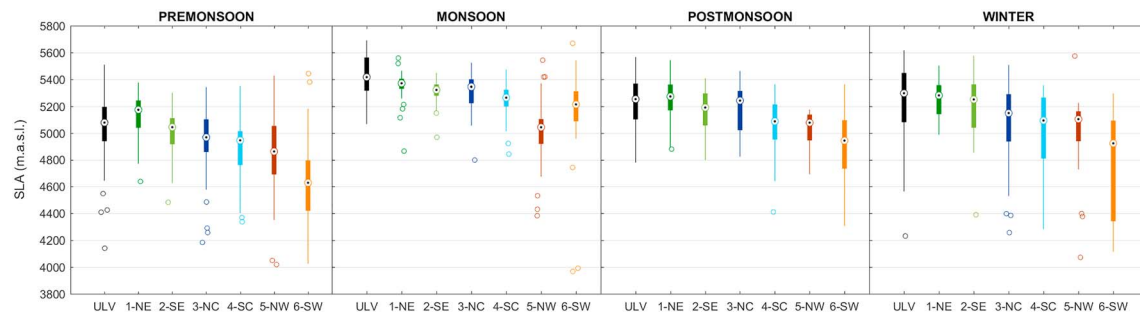


Figure 7. Seasonal SLA boxplots for the entire upper Langtang Valley (ULV) and each subcatchment (e.g., 1-NE corresponds to subcatchment 1 in the northeast). SLA = snow line altitude.

(Figures 6 and 7). The postmonsoon experiences a gradual increment in snow cover (Figure 4), resulting in low annual SLA change (Figure 7) and a stable transition in snow line frequency (Figure 6). In winter, on the other hand, snow cover is sporadic and affects the entire valley, leading to high snow cover frequencies at low altitudes (Figure 6) and a high seasonal SLA variation (Figure 7).

5.3. Snow Line Spatial Patterns

The SLA reaches its minimum in early premonsoon, followed by a heavy retreat in late premonsoon; it peaks in monsoon, and a second (less pronounced) decay and subsequent retreat is observed during postmonsoon, peaking again in early winter (Figure 4).

The analysis of the SLA at the subcatchment scale shows both SLA spatial patterns are consistent across different seasons (Figure 7), and SLA seasonality is also roughly consistent across the catchment (Figure 8). Overall, the SLA ranges from 4,600 to 5,400 m, but apart from the highly variable subcatchment 6, the average annual range does not exceed 500 m for any single subcatchment (Figure 7). While the annual pattern is similar for the different subcatchments, there is a consistent pattern across the valley, with higher monthly SLAs observed in the northeast region (subcatchment 1) and lower SLA values in the western reaches (subcatchments 5 and 6).

Aggregating the SLAs into longitudinal and latitudinal groups (Figure 8), we find clear evidence of two spatial SLA gradients: a longitudinal positive gradient from the west toward the east (Figure 8a); and a latitudinal positive gradient from the south toward the north (Figure 8b). The magnitude of both SLA gradients peaks in late winter and early pre-monsoon, whilst they are least apparent in monsoon.

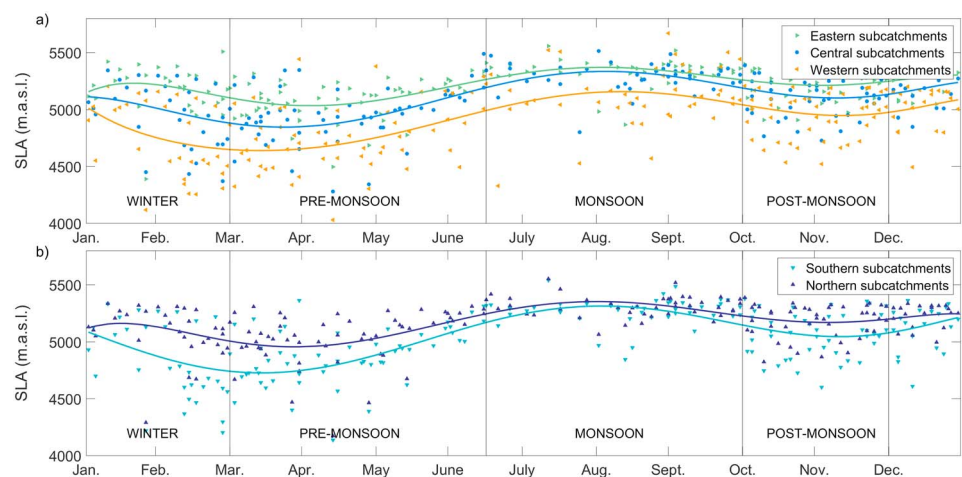


Figure 8. (a) Annual series of SLA values in the eastern (subcatchments 1 and 2), central (subcatchments 3 and 4), and western (subcatchments 5 and 6) reaches of the valley. (b) Annual series of SLA values in the north (subcatchments 1, 3, and 5) and south (subcatchments 2, 4, and 6) reaches of the valley. SLA = snow line altitude.

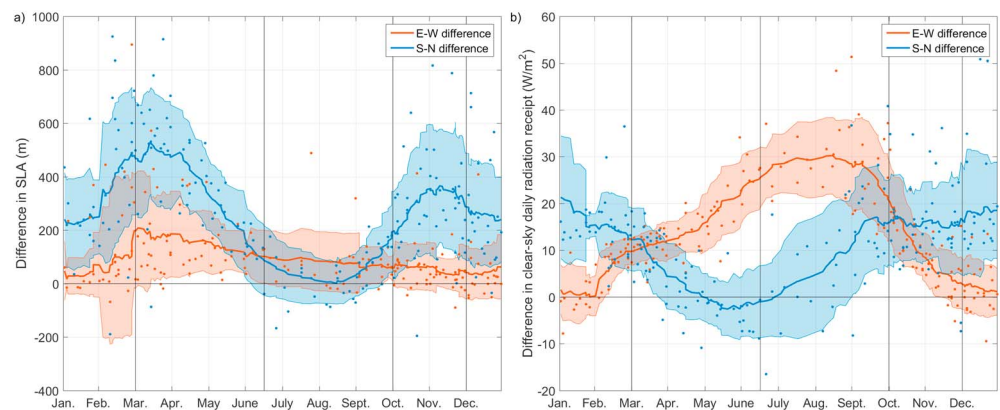


Figure 9. (a) Annual series of SLA differences between East-West (E-W) and South-North (S-N) aspects. (b) Annual series of clear-sky daily radiation receipt difference between E-W and S-N aspects. Scatters show values derived from each scene; lines and shaded bounds correspond to the running mean and running standard deviation (period = 25) of the scatters. SLA = snow line altitude.

6. Discussion

6.1. Aspect-Related Radiation Differences and Snow Line

The aspect dependency evident from seasonal snow cover frequency plots (Figure 5) raises interest in the role of aspect throughout the year and across the basin. We find that east facing SLA is consistently higher than west facing SLA throughout the year (Figure 9a). The maximum differences are recorded in late winter and early premonsoon, whereas the values progressively decrease in late premonsoon, monsoon, and postmonsoon, reaching its minimum during late postmonsoon and early winter. Eventually, the SLA difference starts to increase again in the winter season.

The consistent difference between SLAs in opposite aspect ranges suggests a physical control such as short-wave radiation quantity, and thus, differences in modeled daily clear-sky radiation receipts between opposite aspect ranges (Figure 9b) are analyzed. The seasonality observed in the chart corresponds, to a great extent, with the seasonal behavior of east-west SLA differences (Figure 9a): both the differences between east-west SLA and radiation receipts are lowest in postmonsoon, they inconsistently increase during winter, and high east-west SLA differences in premonsoon are explained by moderate and uniform radiation values across the catchment (Figure 9b). However, the annual minimum east-west SLA differences are observed in the monsoon, in apparent contradiction with the east-west clear-sky radiation differences, which are maximum in monsoon. We attribute this behavior to the monsoonal climate conditions: frequent, heavy cloud cover limits the quantity of spatially variable direct solar radiation, instead leading to high diffuse shortwave radiation, while high temperatures and frequent precipitation events further mitigate snow line differentiation.

Differences between the SLA of north and south facing slopes within each catchment are shown in Figure 9a. The south facing SLA is higher than the north facing SLA during the entire year, with differences generally ranging from 0 to 500 m (Figure 9b). However, strong seasonality in the magnitude is observed: high and maintained differences (from 200 up to 400 m) are observed in postmonsoon, followed by a slight decrease in early winter and a sudden increase in late winter and early premonsoon, after which values start to gradually decrease and drop down to the lowest differences (generally ≤ 200 m) in monsoon.

To a great extent, the south-north SLA differences are explained by the different clear-sky shortwave radiation receipts of south and north aspect ranges (Figure 9b). The position of the Sun is highest in monsoon, and it progressively falls in postmonsoon, reaching its lowest position in winter. This leads to substantial differences between south and north snow line radiation receipts, which explain the high aspect-related SLA differences from postmonsoon until early premonsoon (Figure 9a). However, a slight decrease in magnitude is observed in winter, which is not explained by the radiation quantities. This suggests a secondary physical driver, leading to less winter snow accumulation for north facing slopes, either due to lower snowfall quantities or higher melt rates. Assuming that temperature is controlled by elevation more than aspect, differences in snow melt rates between aspect ranges are mainly controlled by radiative fluxes. As north facing slopes receive the lowest amount of incoming shortwave radiation (Golding & Swanson, 1986), melt rates in north

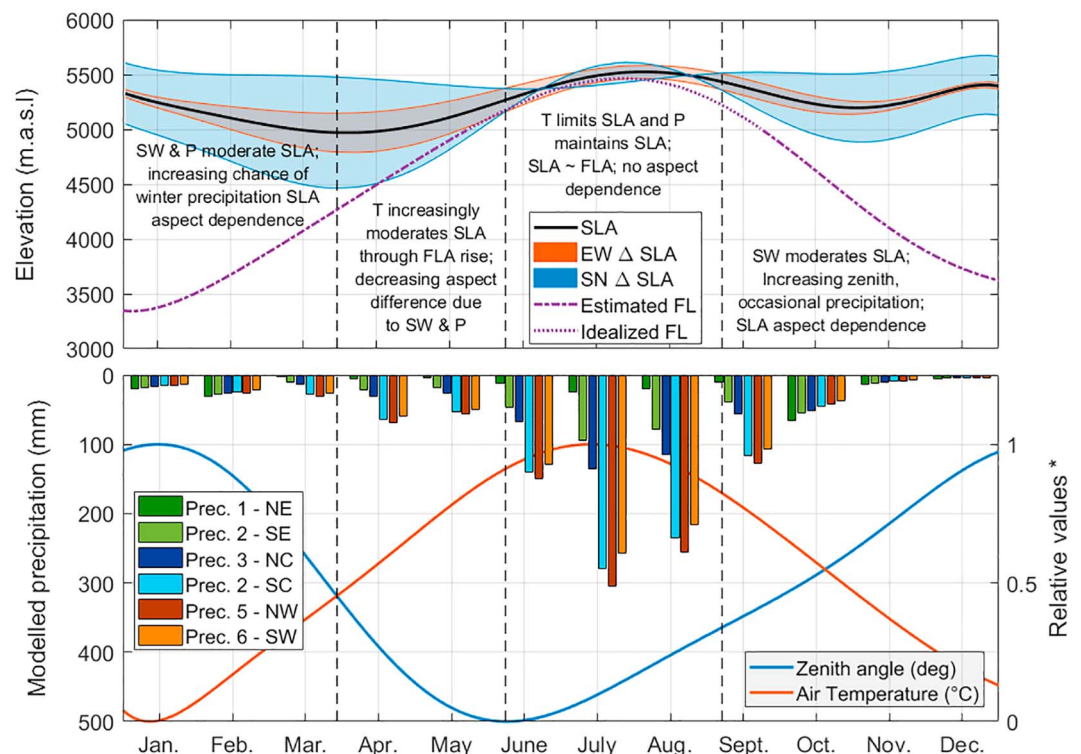


Figure 10. (a) Whole catchment annual series of SLA, opposite aspect (E-W and S-N) SLA differences and estimated/idealized freezing line (FL; P—precipitation, SW—shortwave incoming radiation, T—air temperature). (b) Annual series of zenith angle*, air temperature*, and monthly subcatchment precipitation (*relative values used to show annual patterns conceptually). SLA = snow line altitude.

facing slopes are also expected to be the lowest. Consequently, we expect that snow precipitation might also be a controlling mechanism of the SLA differences between north and south aspect ranges in winter.

Based on Collier and Immerzeel (2015) and Stigter et al. (2017), winter storms are sourced from the east and deposit large quantities of snow, and this is the period where a signal of orographic precipitation is observed: the differences between south and north SLAs are reduced because of the orographic effect, since melt is too low to change things rapidly. This effect is very strong in the east (subcatchment 1), from where winter storms approach but not in the west (subcatchment 6; Figure 5). Our results coincide with those of Jain et al. (2008), which state that less amount of precipitation is received by north facing slopes.

The south facing SLA is particularly higher than the north facing SLA during part of premonsoon and postmonsoon seasons, when incoming shortwave radiation is most influential. In premonsoon, the south-north SLA difference starts to decrease right after peaking in March, clearly responding to a substantial reduction of the difference in radiation receipts between south and north aspect ranges (Figure 9b). However, there is a temporal shift between the decay in magnitude of the SLA differences and the sudden drop of radiation differences and seems to confirm that the snow melt occurs with some delay in north facing slopes (Jain et al., 2008).

Lower radiation receipts by north facing slopes have been noted by several studies (e.g., Golding & Swanson, 1986), but our results provide an independent confirmation of the effect of solar radiation on the SLA, particularly during seasons with low cloud presence, such as premonsoon and postmonsoon (Immerzeel et al., 2014). Eventually, SLA differences between north and south facing slopes are considerably reduced in the monsoon. Again, this can be explained by the sheltering effect of monsoonal frequent cloud cover.

Our results seem to confirm that different aspect ranges may be subjected to slightly different climatic conditions in addition to different clear-sky radiation receipts and support those previously reported by Shiraiwa et al. (1992), which suggest that south and north facing slopes could be exposed to distinct moisture conditions due to wind effects.

6.2. Physical Controls by Season

The integration of our SLA results with observations of key physical parameters (temperature, shortwave radiation, and precipitation) allows us to consider the key processes controlling the observed seasonal and spatial changes in snow cover (Figure 10). In the premonsoon, rising air temperatures and moderate solar angles lead to the highest annual melt rates for the catchment's glaciers (Buri et al., 2016; Steiner et al., 2015), while major precipitation events are only occasional (Immerzeel et al., 2014). This is a self-evident explanation for the substantial SLA variations in that season (Figure 6), when a major SLA increase starts to take place over the entire valley (Figure 4). The premonsoon range of SLAs is accentuated by infrequent but strong winter snowfall events at low elevations, which might also occur at the beginning of this season as the initiation of premonsoon temperature increase exhibits high interannual fluctuations (Morinaga et al., 1987). These events lower the SLA and thus increase the range of SLAs observed in premonsoon. This is illustrated by the low-altitude snow presence for premonsoon (Figure 5). Furthermore, the progressive transition to the monsoon that takes place during the second half of premonsoon (Heynen et al., 2016; Shea et al., 2015) does also contribute to the high SLA span of this season. The progressive transition (in which north and south facing SLA differences are reduced in premonsoon) accounts for the fact that this season exhibits the lowest radiation differences between north and south aspect ranges (Figure 9).

During the monsoon, high temperatures, extensive cloud cover, frequent precipitation events (Immerzeel et al., 2014) and thus relatively stable snow/rain transition altitudes lead to a sharp transition in snow cover frequency (Figure 6). While the season's high solar elevation angles should reduce north-south aspect-related differences, the frequent cloud cover further reduces this influence because diffuse radiation dominates the shortwave budget (Pellicciotti et al., 2011). Consequently, we observe the lowest annual SLA differences between south and north facing slopes (Figure 9a). As the frequent snowfall maintains snow line positions, SLA spatial differences (Figure 8) can be explained by east-west precipitation gradients during occasional premonsoon snowfall events, which lead to a faster retreat of the snow line in the eastern parts of the catchment and therefore a tendency of higher average SLA during monsoon.

Postmonsoon is characterized by fine weather, moderate solar angles, and a constant decrease in air temperature and occasional precipitation events (Figure 10), and the transition from monsoon to postmonsoon is sharp (Shea et al., 2015). This results in a steady SLA behavior for the whole catchment, with consistently lower values than in the monsoon (Figure 7). We infer that occasional snowfall events compensate the melt effect, leading to a low seasonal SLA amplitude across the valley (Figure 6). Thus, melt processes, which would lead to lower SLA stability, seem to play a minor role. However, cloudiness decreases with respect to the monsoon season and therefore aspect-related preferential melt on south facing slopes (Figure 9a) explains increasing SLA differences between north and south aspect ranges (Figure 9b).

From December to February, the climate is characterized by the lowest annual air temperatures, low solar angles, and infrequent but strong precipitation events (Immerzeel et al., 2014), with a high degree of interannual variability (Seko & Takahashi, 1991). The high SLA spread observed in winter (Figure 6) is due to the interannual variability in timing of heavy precipitation events over the season. When snow does fall in winter, it often covers the entire valley and may persist until the following monsoon (Shea et al., 2015), as low temperatures and low solar angles inhibit melt. In some years, large storms leading to area-wide snow cover do not occur before late winter. However, in general terms, aspect-related SLA differences substantially increase during the late stage of the season (February to March), when winter storms have already occurred in most winters (Figure 9a).

We interpret that different processes are controlling the SLA for different seasons (Figure 10). In a spatial sense, the values for different subcatchments tend to diverge during those months when the effect of solid precipitation is dominant (i.e., winter), while melt-controlled periods (i.e., premonsoon) have a convergent effect on the SLAs for the different subcatchments. Monsoonal climate conditions further contribute to the uniformity of SLA throughout the catchment. Eventually, these differences increase only slightly during postmonsoon, when precipitation and melt processes are not too strong and, to a great degree, compensate each other.

Furthermore, the identified SLA spatial patterns (Figure 8) support prior findings of local climatic variability in the Langtang Valley. A west-to-east decrease in precipitation has been observed (Immerzeel et al., 2014), along with further decreases to the north-east (Collier & Immerzeel, 2015; Shiraiwa et al., 1992). Our results suggest the existence of two precipitation gradients across the valley: a dominant longitudinal posi-

tive gradient from east to west and a less pronounced latitudinal positive gradient from north to south. The extreme orography of the valley, acting as a natural barrier for stratus and moisture (Shiraiwa et al., 1992) and even sheltering parts of the valley (Collier & Immerzeel, 2015), would essentially explain such precipitation gradients. These patterns are less pronounced during the monsoon, when south and north SLAs in particular are very similar (Figure 10). During this period, the frequent precipitation, high temperatures, and cloud cover may reduce the dependence of snow cover on position and exposure to radiation.

6.3. The Utility of SLA and SCA

To investigate changes in snow distribution, most studies based on satellite observations analyze snow-covered area (or fraction) rather than SLA (Kaur et al., 2010). Part of the literature bias toward SCA is due to accessibility of the data. First, mapping of SCA from satellite data is fairly established, whereas determination of SLA not only requires careful quality controls and also method validation using a reliable independent source. Second, SCA is a meaningful metric at regional scales even for relatively coarse satellite products (Immerzeel et al., 2009; Lee et al., 2005), whereas measurement of SLA in rugged regions requires higher-resolution source data (Kaur et al., 2010). This results in observation frequency that is generally also much higher for SCA products than for satellite data that could be used to derive SLA. Consequently, global monitoring of regional SCA is routinely undertaken, but SLA is rarely used at all. Intuitively, snow-covered area and SLA are closely related, based on the study area's specific hypsometry. Using an accurate DEM, it would be possible to generate average SLAs from SCA, providing a potential extension of coarser resolution but frequent SCA data (e.g., 500 m data from MODIS) to a higher resolution at a study site.

However, SLA measurement offers some key advantages over SCA for understanding snow processes at a site, as it provides a detailed spatial description of snow presence from a single metric. Furthermore, the fact that SLA is expressed in absolute altitude units enables comparisons between nearby sites or regions with different geomorphology but comparable climate (e.g., to assess the climatic differences). The processing applied in this study produces a set of snow cover boundary points, enabling the investigation of broad spatial differences across the study site as well as fine differences between aspect ranges. More importantly, outliers are readily identifiable from this set of points and have implications for data quality, indicating potential misidentification of snow/ice. Snow line outliers are useful for identifying physical processes of snow redistribution. In the rugged Himalayas, avalanches are a regular occurrence and can significantly modify the surface processes of glaciers (Inoue, 1977; Scherler et al., 2011) as well as catchment hydrology (Uhlenbrook, 2006) but are very difficult to study. Avalanche deposits are very clearly depicted by the snow cover maps (i.e., the source of both SCA and SLA metrics). However, as the SCA is often expressed as an integrated signal over a large domain, single avalanche events are poorly represented. Conversely, the SLA can easily be a statistical metric at the subcatchment or even aspect scale; thus, the local change due to a single (large) avalanche can be significant and more readily observable.

SLA data are also potentially more advantageous than SCA for use in modeling at the catchment scale. SCA is often used in calibration to ensure that models are predicting snow well (Ragetti et al., 2015; Stigter et al., 2017). However, the magnitude of SCA variations does not only relate to meteorological conditions but also depends on the site's topography, that is, geometry of snow-covered areas and orographic features. Conversely, SLA, while indirectly controlled by topography, responds directly to near-surface meteorology (McFadden et al., 2011). At much coarser scales, however, SCA is useful for determining subgrid short-wave radiation balance, while SLA is not particularly useful in this regard. The two metrics are strongly complementary, and the use of snow lines provides additional insights into local snow cover dynamics.

While we use Landsat TM and ETM+ historic data sets to delineate snow lines, there is a growing range of free, quality-assured and fit-for-purpose satellite-derived Earth-observation products (e.g., Landsat 8, Sentinel 2, Planet Skysat) that can be used to monitor snow line dynamics in a similar way and would definitely be suitable for a follow-on study. In fact, the refined characteristics of some of these products (e.g., higher temporal resolution, more spectral bands and/or higher spatial resolution) provide opportunities for increasing the accuracy of snow line delineation. Further opportunities also arise from using synthetic-aperture radar products such as those provided by Sentinel-1, which is able to penetrate clouds and can also differentiate between wet and dry snow. This could be extremely useful to additionally identify areas of ablation and accumulation on glaciers, which can be directly related to the freezing line.

7. Conclusions

In this work, we have used 15 years of Landsat TM and ETM+ data to study the spatial and seasonal variation of the snow line and its control mechanisms in a Himalayan catchment. The relatively high spatial resolution offered by Landsat imagery enabled us to obtain a detailed delineation of the snow line in spite of data-quality challenges.

Among topographic and climatic conditions, precipitation has been shown to be one of the main control mechanisms of the SLA dynamics. We have identified two SLA spatial gradients, which we have attributed to the effect of spatially variable precipitation. Eastern reaches of the valley have a higher SLA than western areas, and, to a lesser extent, SLA decreases from the north toward the southern parts of the upper Langtang Valley. These results give an independent confirmation of the regional variation of precipitation found in previous studies (Immerzeel et al., 2014; Ragetti et al., 2015; Shiraiwa et al., 1992) and indicate the existence of an east-west positive precipitation gradient. Likewise, our results suggest the occurrence of a secondary positive precipitation gradient from the north toward the south.

We also find that topographic aspect has a remarkable effect on the SLA: first, the SLA is higher for east facing slopes than for west facing slopes, and second, the SLA is higher for south facing slopes than for north facing slopes. These patterns are consistent over the year and across catchments and are generally attributed to differences in clear-sky radiation receipts. However, the SLA differences between both east-west and south-north aspect ranges exhibit marked seasonality, which suggests that different processes may control aspect-related snow cover differences for each season: incoming shortwave radiation is dominant in pre-monsoon and postmonsoon, while sporadic orographic precipitation leads to a less consistent behavior in winter. During summer, snow cover is less dependent on aspect since the SLA is mostly controlled by the altitude of the snow/rain transition.

We have found that SLA seasonal dynamics respond to different principal controls for each season. In particular, SLA variations in premonsoon are related to melt processes; occasional snowfall events slightly outweigh melting effects in postmonsoon, leading to a smooth SLA decrease; accumulation favors SLA instability in winter and the SLA remains highly stable in monsoon. Finally, the SLA differences between subcatchments tend to decrease in premonsoon and monsoon, increase in winter, and they remain steady in postmonsoon.

Based on the results of this work, we conclude that the SLA has a strong potential for understanding local-scale snow cover dynamics. The greater level of detail that the SLA provides compared to other snow cover metrics (e.g., SCA) enables the spatial analysis of snow cover, and both metrics are highly complementary for catchment-scale studies. We have found that the use of the SLA is particularly advantageous for the study of snow cover spatial and aspect-related differences, as well as their controlling mechanisms. Furthermore, we suggest that modeling studies take advantage of the SLA data as calibration and/or validation data set, in order to further investigate the relations between snow cover, meteorology, and topography and in order to assess the role of catchment-scale snow cover dynamics for water resources.

Acknowledgments

This work has been partly funded by the Swiss National Science Foundation project UNCOMUN (SNF 200021L146761). The authors gratefully acknowledge the USGS and NASA Land Processes Distributed Active Archive Center for free access to Landsat and SRTM data and thank ICIMOD for maintaining the weather station at Kyanjing. The data sets generated and/or analyzed during the current study are available in Zenodo online (Girona-Mata et al., 2019).

References

- Benxing, Z., Watanabe, O., & D. Mulmi, D. (1984). Glacier features and their variations in the Langtang Himal region of Nepal. *Bulletin of Glaciological Research*, 2, 121–127.
- Bolch, T., Kulkarni, A. V., Kääb, A., Huggel, C., Paul, F., Cogley, J. G., et al. (2012). The state and fate of Himalayan glaciers. *Science*, 336(6079), 310–314. <https://doi.org/10.1126/science.1215828>
- Bonekamp, P. N. J., Collier, E., & Immerzeel, W. W. (2018). The impact of spatial resolution, land use, and spinup time on resolving spatial precipitation patterns in the Himalayas. *Journal of Hydrometeorology*, 19, 1565–1581. <https://doi.org/10.1175/JHM-D-0212.1-17-0212.1>
- Buri, P., Pellicciotti, F., Steiner, J. F., Miles, E. S., & Immerzeel, W. W. (2016). A grid-based model of backwasting of supraglacial ice cliffs on debris-covered glaciers. *Annals of Glaciology*, 57(71), 199–211. <https://doi.org/10.3189/2016AoG71A059>
- Burke, H.-H. K., Bowley, C. J., & Barnes, J. C. (1984). Determination of snowpack properties from satellite passive microwave measurements. *Remote Sensing of Environment*, 15(1), 1–20. [https://doi.org/10.1016/0034-4257\(84\)90048-8](https://doi.org/10.1016/0034-4257(84)90048-8)
- Burns, P., & Nolin, A. (2014). Using atmospherically-corrected Landsat imagery to measure glacier area change in the Cordillera Blanca, Peru from 1987 to 2010. *Remote Sensing of Environment*, 140, 165–178. <https://doi.org/10.1016/j.rse.2013.08.026>
- Collier, E., & Immerzeel, W. W. (2015). High-resolution modeling of atmospheric dynamics in the Nepalese Himalaya. *Journal of Geophysical Research: Atmospheres*, 120, 9882–9896. <https://doi.org/10.1002/2015JD023266>
- Corripio, J. G. (2003). Vectorial algebra algorithms for calculating terrain parameters from DEMs and solar radiation modelling in mountainous terrain. *International Journal of Geographical Information Science*, 17, 1–23. <https://doi.org/10.1080/713811744>
- Dahe, Q., Shiyin, L., & Peiji, L. (2006). Snow cover distribution, variability, and response to climate change in western China. *Journal of Climate*, 19, 1820–1833. <https://doi.org/10.1175/JCLI3694.1>

- Dedieu, J. P., Lessard-Fontaine, A., Ravazzani, G., Cremonese, E., Shalpykova, G., & Beniston, M. (2014). Shifting mountain snow patterns in a changing climate from remote sensing retrieval. *Science of the Total Environment*, 493, 1267–1279. <https://doi.org/10.1016/j.scitotenv.2014.04.078>
- Deems, J. S., Fassnacht, S. R., & Elder, K. J. (2006). Fractal distribution of snow depth from LiDAR data. *Journal of Hydrometeorology*, 7(2), 285–297. <https://doi.org/10.1175/JHM487.1>
- Dietz, A. J., Kuenzer, C., Gessner, U., & Dech, S. (2012). Remote sensing of snow — a review of available methods. *International Journal of Remote Sensing*, 33(13), 4094–4134. <https://doi.org/10.1080/01431161.2011.640964>
- Dozier, J. (1989). Spectral signature of Alpine snow cover from the LANDSAT Thematic Mapper. *Remote Sensing of Environment*, 28, 9–22. [https://doi.org/10.1016/0034-4257\(89\)90101-6](https://doi.org/10.1016/0034-4257(89)90101-6)
- Fausto, R. S., & the PROMICE team (2017). The Greenland ice sheet-snowline elevations at the end of the melt seasons from 2000 to 2017. *Geological Survey of Denmark and Greenland Bulletin*, 41, 71–74.
- Girona-Mata, M., Miles, E. S., Ragetti, S., & Pellicciotti, F. (2019). Data used in manuscript "High-resolution snowline delineation from Landsat imagery to infer snow cover controls in a Himalayan catchment". [Data set]. Zenodo. <http://doi.org/10.5281/zenodo.3256543>
- Golding, D. L., & Swanson, R. H. (1986). Snow distribution patterns in clearings and adjacent forest. *Water Resources Research*, 22, 1931–1940. <https://doi.org/10.1029/WR022i013p01931>
- Gurung, D. R., Maharjan, S. B., Shrestha, A. B., Shrestha, M. S., Bajracharya, S. R., & Murthy, M. S. R. (2017). Climate and topographic controls on snow cover dynamics in the Hindu Kush Himalaya. *International Journal of Climatology*, 37, 3873–3882. <https://doi.org/10.1002/joc.4961>
- Härer, S., Bernhardt, M., Siebers, M., & Schulz, K. (2018). On the need for a time- and location-dependent estimation of the NDSI threshold value. *The Cryosphere*, 12(5), 1629–1642. <https://doi.org/10.5194/tc-12-1629-2018>
- Hall, D. K., Riggs, G. A., & Salomonson, V. V. (1995). Development of methods for mapping global snow cover using moderate resolution imaging spectroradiometer data. *Remote Sensing of Environment*, 54, 127–140. [https://doi.org/10.1016/0034-4257\(95\)00137-P](https://doi.org/10.1016/0034-4257(95)00137-P)
- Her, Y., Heatwole, C. D., & Kang, M. S. (2015). Interpolating SRTM elevation data to higher resolution to improve hydrologic analysis. *Journal of the American Water Resources Association*, 51(4), 1072–1087. <https://doi.org/10.1111/jawr.12287>
- Heynen, M., Miles, E. S., Ragetti, S., Buri, P., Immerzeel, W. W., & Pellicciotti, F. (2016). Air temperature variability in a high-elevation Himalayan catchment. *Annals of Glaciology*, 57(71), 212–222. <https://doi.org/10.3189/2016AoG71A076>
- Huss, M., Sold, L., Hoelzle, M., Stokvis, M., Salzmann, N., Farinotti, D., & Zemp, M. (2013). Towards remote monitoring of sub-seasonal glacier mass balance. *Annals of Glaciology*, 54(63), 75–83. <https://doi.org/10.3189/2013AoG63A427>
- Immerzeel, W. W., Droogers, P., de Jong, S. M., & Bierkens, M. F. P. (2009). Large-scale monitoring of snow cover and runoff simulation in Himalayan river basins using remote sensing. *Remote Sensing of Environment*, 113, 40–49. <https://doi.org/10.1016/j.rse.2008.08.010>
- Immerzeel, W. W., Pellicciotti, F., & Bierkens, M. F. P. (2013). Rising river flows throughout the twenty-first century in two Himalayan glacierized watersheds. *Nature Geoscience*, 6(9), 742–745. <https://doi.org/10.1038/ngeo1896>
- Immerzeel, W. W., Pellicciotti, F., & Shrestha, A. B. (2012). Glaciers as a proxy to quantify the spatial distribution of precipitation in the Hunza Basin. *Mountain Research and Development*, 32(1), 30–38. <https://doi.org/10.1659/MRD-JOURNAL-D-11-00097.1>
- Immerzeel, W. W., Petersen, L., Ragetti, S., & Pellicciotti, F. (2014). The importance of observed gradients of air temperature and precipitation for modeling runoff from a glacierized watershed in the Nepalese Himalayas. *Water Resources Research*, 50, 2212–2226. <https://doi.org/10.1002/2013WR014506>
- Inoue, J. (1977). Mass budget of Khumbu Glacier. *Journal of the Japanese Society of Snow and Ice*, 39(Special), 15–19. <https://doi.org/10.5331/seppyo.39.Special15>
- Iqbal, M. (1983). *An introduction to solar radiation* (1st ed.): Academic Press. ISBN: 9780323151818.
- Jain, S. K., Goswami, A., & Saraf, A. K. (2008). Role of elevation and aspect in snow distribution in Western Himalaya. *Water Resources Management*, 23(1), 71–83. <https://doi.org/10.1007/s11269-008-9265-5>
- Jarvis, A., Reuter, H. I., & Nelson, A. (2008). Hole-filled SRTM for the globe Version 4, available from the CGIAR-CSI SRTM 90m Database.
- Kapnick, S., & Hall, A. (2011). Causes of recent changes in western North American snowpack. *Climate Dynamics*, 38(9–10), 1885–1899. <https://doi.org/10.1007/s00382-011-1089-y>
- Kaur, R., Kulkarni, A. V., & Chaudhary, B. S. (2010). Using RESOURCESAT-1 data for determination of snow cover and snowline altitude, Baspa Basin, India. *Annals of Glaciology*, 51(54), 9–13. <https://doi.org/10.3189/172756410791386625>
- Klein, A. G., & Isacks, B. L. (1999). Spectral mixture analysis of Landsat thematic mapper images applied to the detection of the transient snowline on tropical Andean glaciers. *Global and Planetary Change*, 22(1–4), 139–154. [https://doi.org/10.1016/S0921-8181\(99\)00032-6](https://doi.org/10.1016/S0921-8181(99)00032-6)
- Kotchenova, S. Y., & Vermote, E. F. (2007). Validation of a vector version of the 6S radiative transfer code for atmospheric correction of satellite data. Part II. Homogeneous Lambertian and anisotropic surfaces. *Applied optics*, 46(20), 4455–4464. <https://doi.org/10.1364/AO.46.004455>
- Kulkarni, A. V., Singh, S. K., Mathur, P., & Mishra, V. D. (2006). Algorithm to monitor snow cover using AWiFS data of RESOURCESAT-1 for the Himalayan region. *International Journal of Remote Sensing*, 27(12), 2449–2457. <https://doi.org/10.1080/01431160500497820>
- Lee, S., Klein, A. G., & Over, T. M. (2005). A comparison of MODIS and NOHRSC snow-cover products for simulating streamflow using the Snowmelt Runoff Model. *Hydrological Processes*, 19(15), 2951–2972. <https://doi.org/10.1002/hyp.5810>
- Lutz, A. F., Immerzeel, W. W., Shrestha, A. B., & Bierkens, M. F. P. (2014). Consistent increase in High Asia's runoff due to increasing glacier melt and precipitation. *Nature Climate Change*, 4(7), 587–592. <https://doi.org/10.1038/nclimate2237>
- Maskey, S., Uhlenbrook, S., & Ojha, S. (2011). An analysis of snow cover changes in the Himalayan region using MODIS snow products and in-situ temperature data. *Climatic Change*, 108(1–2), 391–400. <https://doi.org/10.1007/s10584-011-0181-y>
- McFadden, E. M., Ramage, J., & Rodbell, D. T. (2011). Landsat TM and ETM+ derived snowline altitudes in the Cordillera Huayhuash and Cordillera Raura, Peru, 1986–2005. *The Cryosphere*, 5, 419–430. <https://doi.org/10.5194/tc-5-419-2011>
- Melvold, K., & Skaugen, T. (2013). Multiscale spatial variability of lidar-derived and modeled snow depth on Hardangervidda, Norway. *Annals of Glaciology*, 54(62), 273–281. <https://doi.org/10.3189/2013AoG62A161>
- Miles, E. S., Willis, I. C., Arnold, N. S., Steiner, J., & Pellicciotti, F. (2017). Spatial, seasonal and interannual variability of supraglacial ponds in the Langtang Valley of Nepal, 1999–2013. *Journal of Glaciology*, 63(237), 88–105. <https://doi.org/10.1017/jog.2016.120>
- Mishra, B., Babel, M. S., & Tripathi, N. K. (2013). Analysis of climatic variability and snow cover in the Kaligandaki River Basin, Himalaya, Nepal. *Theoretical and Applied Climatology*, 116(3–4), 681–694. <https://doi.org/10.1007/s00704-013-0966-1>
- Molotch, N. P., & Bales, R. C. (2006). SNOTEL representativeness in the Rio Grande headwaters on the basis of physiographics and remotely sensed snow cover persistence. *Hydrological Processes*, 20(4), 723–739. <https://doi.org/10.1002/hyp.6128>
- Molotch, N. P., & Meromy, L. (2014). Physiographic and climatic controls on snow cover persistence in the Sierra Nevada Mountains. *Hydrological Processes*, 28(16), 4573–4586. <https://doi.org/10.1002/hyp.10254>

- Morinaga, Y., Seko, K., & Takahashi, S. (1987). Seasonal variation of snowline in Langtang Valley, Nepal Himalayas, 1985–1986. *Bulletin of Glaciological Research*, 5, 49–53. [eng.](#)
- Painter, T. H., Rittger, K., McKenzie, C., Slaughter, P., Davis, R. E., & Dozier, J. (2009). Retrieval of subpixel snow covered area, grain size, and albedo from MODIS. *Remote Sensing of Environment*, 113(4), 868–879. <https://doi.org/10.1016/j.rse.2009.01.001>
- Pellicciotti, F., Raschle, T., Huerlimann, T., Carenzo, M., & Burlando, P. (2011). Transmission of solar radiation through clouds on melting glaciers: A comparison of parameterizations and their impact on melt modelling. *Journal of Glaciology*, 57(202), 367–381. <https://doi.org/10.3189/002214311796406013>
- Pellicciotti, F., Stephan, C., Miles, E. S., Herreid, S., Immerzeel, W. W., & Bolch, T. (2015). Mass balance changes of the debris-covered glaciers in the Langtang Himal in Nepal between 1974 and 1999. *Journal of Glaciology*, 61(226), 373–386. <https://doi.org/10.3189/2015JoG13J237>
- Pelto, M. (2011). Utility of late summer transient snowline migration rate on Taku Glacier, Alaska. *The Cryosphere*, 5(4), 1127–1133. <https://doi.org/10.5194/tc-5-1127-2011>
- Pomeroy, J. W., Marks, D., Link, T., Ellis, C., Hardy, J., Rowlands, A., & Granger, R. (2009). The impact of coniferous forest temperature on incoming longwave radiation to melting snow. *Hydrological Processes*, 23, 2513–2525. <https://doi.org/10.1002/hyp.7325>
- et al. (2017). Glacier snowline determination from terrestrial laser scanning intensity data. *Geosciences*, 7(3), 60. <https://doi.org/10.3390/geosciences7030060>
- Ragetti, S., Pellicciotti, F., Immerzeel, W. W., Miles, E. S., Petersen, L., Heynen, M., et al. (2015). Unraveling the hydrology of a Himalayan catchment through integration of high resolution in situ data and remote sensing with an advanced simulation model. *Advances in Water Resources*, 78, 94–111. <https://doi.org/10.1016/j.advwatres.2015.01.013>
- Rango, A., & Itten, K. I. (1976). Satellite potentials in snow cover monitoring and runoff prediction. *Nordic Hydrology*, 7(4), 209–230. <https://doi.org/10.2166/nh.1976.0014>
- Rittger, K., Painter, T. H., & Dozier, J. (2013). Assessment of methods for mapping snow cover from MODIS. *Advances in Water Resources*, 51, 367–380. <https://doi.org/10.1016/j.advwatres.2012.03.002>
- Rosenthal, W., & Dozier, J. (1996). Automated mapping of montane snow cover at subpixel resolution from the Landsat Thematic Mapper. *Water Resources Research*, 32(1), 115–130. <https://doi.org/10.1029/95WR02718>
- Scherler, D., Bookhagen, B., & Strecker, M. R. (2011). Hillslope-glacier coupling: The interplay of topography and glacial dynamics in High Asia. *Journal of Geophysical Research*, 116, F02019. <https://doi.org/10.1029/2010JF001751>
- Seidel, K., Ehrler, C., Martinec, J., & Turpin, O. (1997). Derivation of statistical snowline from high resolution snow cover mapping. In *Proceedings of the 1st EARSeL Workshop on Remote Sensing of Land Ice and Snow, University of Freiburg, Germany, 17-18 April 1997*, European Association of Remote-Sensing Laboratories, Paris, pp. 31–36.
- Seko, K. (1987). Seasonal variation of altitudinal dependence of precipitation in Langtang Valley, Nepal Himalayas. *Bulletin of Glacier Research*, 5, 41–47.
- Seko, K., & Takahashi, S. (1991). Characteristics of winter precipitation and its effect on glaciers in the Nepal Himalaya. *Bulletin of Glaciological Research*, 9, 9–16.
- Shea, J. M., Immerzeel, W. W., Wagnon, P., Vincent, C., & Bajracharya, S. (2015). Modelling glacier change in the Everest region, Nepal Himalaya. *The Cryosphere*, 9(3), 1105–1128. <https://doi.org/10.5194/tc-9-1105-2015>
- Shea, J. M., Menounos, B., Moore, R. D., & Tennant, C. (2013). An approach to derive regional snow lines and glacier mass change from MODIS imagery, western North America. *The Cryosphere*, 7(2), 667–680. <https://doi.org/10.5194/tc-7-667-2013>
- Shea, J. M., Wagnon, P., Immerzeel, W. W., Biron, R., Brun, F., & Pellicciotti, F. (2015). A comparative high-altitude meteorological analysis from three catchments in the Nepalese Himalaya. *International Journal of Water Resources Development*, 31(2), 174–200. <https://doi.org/10.1080/07900627.2015.1020417>
- Shi, J., & Dozier, J. (1993). Measurements of snow- and glacier-covered areas with single-polarization SAR. *Annals of Glaciology*, 17, 72–76. <https://doi.org/10.3189/S0260305500012635>
- Shiraiwa, A., Takayuki, Ueno, K., & Yamada, T. (1992). Distribution of mass input on glaciers in the Langtang Valley, Nepal Himalayas. *Bulletin of Glaciological Research*, 10, 21–30.
- Shrestha, A. B., & Aryal, R. (2010). Climate change in Nepal and its impact on Himalayan glaciers. *Regional Environmental Change*, 11(S1), 65–77. <https://doi.org/10.1007/s10113-010-0174-9>
- Sorman, A. A., Uysal, G., & Sensoy, A. (2019). Probabilistic snow cover and ensemble streamflow estimations in the Upper Euphrates Basin. *Journal of Hydrology and Hydromechanics*, 67(1), 82–92. <https://doi.org/10.2478/johh-2018-0025>
- Steiner, J. F., Pellicciotti, F., Buri, P., Miles, E. S., Immerzeel, W. W., & Reid, T. D. (2015). Modelling ice-cliff backwasting on a debris-covered glacier in the Nepalese Himalaya. *Journal of Glaciology*, 61(229), 889–907. <https://doi.org/10.3189/2015JoG14J194>
- Stigter, E. E., Wanders, N., Saloranta, T. M., Shea, J. M., Bierkens, M. F. P., & Immerzeel, W. W. (2017). Assimilation of snow cover and snow depth into a snow model to estimate snow water equivalent and snowmelt runoff in a Himalayan catchment. *The Cryosphere*, 11, 1647–1664. <https://doi.org/10.5194/tc-11-1647-2017>
- Tahir, A. A., Chevallier, P., Arnaud, Y., & Ahmad, B. (2011). Snow cover dynamics and hydrological regime of the Hunza River basin, Karakoram Range, Northern Pakistan. *Hydrology and Earth System Sciences*, 15(7), 2275–2290. <https://doi.org/10.5194/hess-15-2275-2011>
- Uhlenbrook, S. (2006). Catchment hydrology—a science in which all processes are preferential. *Hydrological Processes*, 20(16), 3581–3585. <https://doi.org/10.1002/hyp.6564>
- Uppala, S. M., Kallberg, P. W., Simmons, A. J., Andrae, U., Bechtold, V. D., M., F., et al. (2005). The ERA-40 re-analysis. *Quarterly Journal of the Royal Meteorological Society*, 131, 2961–3012. <https://doi.org/10.1256/qj.04.176>
- Wang, R., Yao, Z., Liu, Z., Wu, S., Jiang, L., & Wang, L. (2015). Snow cover variability and snowmelt in a high altitude ungauged catchment. *Hydrological Processes*, 29(17), 3665–3676. <https://doi.org/10.1002/hyp.10472>
- Yasunari, T., & Inoue, J. (1978). Characteristics of monsoonal precipitation around peaks and ridges in Shorong and Khumbu Himal. *Journal of the Japanese Society of Snow and Ice*, 40, 26–32. <https://doi.org/10.5331/seppyo.40.Special&urlscore;26>
- Zelazowski, P., Sayer, A. M., Thomas, G. E., & Grainger, R. G. (2011). Reconciling satellite-derived atmospheric properties with fine-resolution land imagery: Insights for atmospheric correction. *Journal of Geophysical Research*, 116, D18308. <https://doi.org/10.1029/2010JD015488>